Photoinduced anomalous Hall effect in two-dimensional transition metal dichalcogenides

Phuong X. Nguyen and Wang-Kong Tse ⓘ

Department of Physics and Astronomy, The University of Alabama, Tuscaloosa, Alabama 35487, USA

A circularly polarized ac pump field illuminated near resonance on two-dimensional transition metal dichalcogenides (TMDs) produces an anomalous Hall effect in response to a dc bias field. In this work, we develop a theory for this photoinduced anomalous Hall effect in undoped TMDs irradiated by a strong coherent laser field. The strong field renormalizes the equilibrium bands and opens up a dynamical energy gap where single-photon resonance occurs. The resulting photon dressed states, or Floquet states, are treated within the rotating-wave approximation. A quantum kinetic equation approach is developed to study the nonequilibrium density matrix and time-averaged transport currents under the simultaneous influence of the strong ac pump field and the weak dc probe field. Dissipative effects are taken into account in the kinetic equation that captures relaxation and dephasing. The photoinduced longitudinal and Hall conductivities display notable resonant signatures when the pump field frequency reaches the spin-split interband transition energies. Rather than valley polarization, we find that the anomalous Hall current is mainly driven by the intraband response of photon-dressed electron populations near the dynamical gap at both valleys, accompanied by a smaller contribution due to the interband response. These findings highlight the importance of photon-dressed bands and nonequilibrium distribution functions in achieving a proper understanding of the photoinduced anomalous Hall effect in a strong pump field.

I. INTRODUCTION

Since the discovery of graphene [1], van der Waals materials have emerged as a broad family of two-dimensional (2D) layered materials with diverse physical properties ranging from semimetals, semiconductors, and insulators to 2D ferromagnets and superconductors [2]. Two-dimensional transition metal dichalcogenides (TMDs) (e.g., MoS_2, WS_2, $MoSe_2$, and WSe_2) are van der Waals semiconductors with a band gap within the visible spectrum. In monolayers, TMDs exhibit broken spatial inversion symmetry combined with strong spin-orbit interaction, resulting in a large valence-band splitting appearing across the direct gaps at the valleys K and K' [3] with inherently coupled spin and valley degrees of freedom [4]. Through the valley selection rule, carriers near the valence-band edge at each of the valleys couple preferentially to light with a definite circular polarization, allowing them to be selectively excited to the conduction band. For frequencies above the band gap, the optical excitation creates a carrier population imbalance between the two valleys, i.e., a valley polarization [5].

If the system is additionally driven by a dc electric field, valley-resolved photovoltaic transport occurs. In particular, an anomalous Hall effect will result from the net transverse charge current due to unbalanced population of photoexcited K and K' carriers [6,7]. A similar Hall effect, caused by photoinduced spin polarization, has also been predicted [8] in semiconductor systems due to spin-orbit coupling and observed [9–12] in III-V semiconductor structures, Bi_2Se_3 topological insulator thin film [13], and few-layer WTe_2 Weyl

semimetal [14]. In TMDs, this photoinduced anomalous Hall effect (AHE) has been recently observed in illuminated samples of monolayer MoS_2 as well as bilayer MoS_2 placed under an out-of-plane electric field [15,16]. It has also been recently observed in illuminated samples of exfoliated graphene [17,18], in which the Hall effect is purely due to optically induced Berry curvature.

Early theoretical treatments on the photoinduced Hall effect in TMDs have been largely focused on the role of valley selection rules and Berry curvatures obtained from the equilibrium bands, with the tacit assumption that the optical excitation is sufficiently weak that the electronic band structure remains unaltered under irradiation. Hall transport in the regime of strong optical excitations, which can reveal rich quantum dynamics through photon-dressing effects and are readily realizable in experiments, has received increasing theoretical attention [19–24]. In a recent experiment [25], dynamic Stark shift of the bands has been observed in WS_2 under a strong optical pump field with subgap frequency. When the pump frequency is above the band gap, hybridization between the photon-dressed valence and conduction bands generates a dynamical gap [26,27]. The hybridized states, which are also known as Floquet states, have not yet been observed in TMDs but have been directly observed in topological insulator surface states [28,29]. The realization of Floquet states provides a means to realize many interesting nonequilibrium phenomena [30], such as Floquet topological phases [31,32], Floquet control of exchange interaction [33,34] and tunneling [35], and Floquet time crystals [36].

Under strong optical excitation by the pump field, the valley-resolved Hall effect is influenced by the photon renormalization of the electronic bands as well as nonequilibrium carrier kinetics [37]. In this work, we provide a density matrix formulation for photoinduced valley Hall transport that allows us to treat the photon-dressed bands and carrier kinetics in a single framework. Our theory is developed using the rotating-wave approximation, which provides better analytic insights compared to full numerical solutions, in the regime of near resonance and weak coupling where multiphoton effects are unimportant [24]. Band populations and interband coherences are obtained in a transparent manner from the solution of the kinetic equation of the density matrix. These are then used to compute the photoinduced valley polarization and longitudinal and Hall photoconductivities. Our findings reveal that the physical picture behind the photoinduced anomalous Hall effect is much more nuanced in a strong laser field than the commonly assumed picture of valley population imbalance, due to the formation of different photon-dressed bands at the two valleys.

Our paper is organized as follows. Section II lays out the model of our system and discusses the photon-induced renormalization of the equilibrium band structure. We then introduce the density matrix formalism and the kinetic equation governing its dynamics in Sec. III. In Secs. IV and V, we solve the kinetic equation and obtain the density matrix of the pumped system, first in the absence and then in the presence of the dc electric field. Section VI then presents the derivation of the photovoltaic longitudinal and Hall currents and our numerical results of the photoconductivities, followed by our conclusion in Sec. VII.

II. MODEL OF TMD COUPLED TO AN OPTICAL PUMP FIELD

The low-energy Hamiltonian of a 2D TMD is given by [4]

$$H_0 = v(\tau k_x \sigma_x + k_y \sigma_y) + \left(\hat{\Delta} - \frac{\lambda \tau}{2} s_z\right)\sigma_z + \frac{\lambda \tau}{2} s_z, \quad (1)$$

where $\boldsymbol{\sigma}$ denotes the vector of Pauli matrices in the pseudospin basis capturing the d-orbital states of the transition metal element, $2\hat{\Delta}$ is the band-gap energy, v is the band velocity, 2λ is the spin-orbit splitting of the valence bands, $\tau = \pm 1$ is the valley index for K and K', respectively, and $s_z = \pm 1$ is the spin index for up and down. In the vicinity of each valley, the low-energy physics is described by two copies of the spin-resolved Dirac Hamiltonian with a band gap $2\Delta_{1,2} = 2\hat{\Delta} \mp \lambda$. In this paper, we take MoS$_2$ as the prototypical example of TMDs, and we use the corresponding values [4] of band gap $2\hat{\Delta} = 1.66$ eV, spin-orbit splitting $2\lambda = 0.15$ eV, and band velocity $v = 5.35 \times 10^5$ ms^{-1} for our numerical calculations.

We can develop our theory for one spin s and one valley τ and obtain the total photovoltaic current at the end by summing the contributions from both spins and both valleys. Dropping the inessential energy shift from the last term, Eq. (1) takes the typical form of a massive Dirac Hamiltonian

$$H_0 = v(\tau k_x \sigma_x + k_y \sigma_y) + \Delta \sigma_z, \quad (2)$$

where $\Delta = \hat{\Delta} - \tau s_z \lambda/2$, which takes the two values $\Delta_{1,2}$ corresponding to $\tau s_z = \pm 1$. Diagonalizing Eq. (2) gives the conduction-band (+) and valence-band (−) energy $\pm \alpha_k = \pm\sqrt{(vk)^2 + \Delta^2}$, and the corresponding spinor wave functions,

$$\chi_{k+} = \begin{bmatrix} \cos(\theta_k/2) \\ \sin(\theta_k/2)e^{i\tau\phi} \end{bmatrix}, \quad \chi_{k-} = \begin{bmatrix} -\sin(\theta_k/2) \\ \cos(\theta_k/2)e^{i\tau\phi} \end{bmatrix}, \quad (3)$$

where we have defined $\cos\theta_k = \Delta/\alpha_k$, $\sin\theta_k = \tau vk/\alpha_k$, $\tan\phi = k_y/k_x$, and $k = \sqrt{k_x^2 + k_y^2}$.

The pump field laser is described by an ac electric field $\boldsymbol{E} = E_0(\cos\omega t \hat{x} + \mu \sin\omega t \hat{y})$, in which $\mu = \pm 1$ denotes the left and right circular polarization. The light-matter interaction Hamiltonian follows from the minimal coupling $\boldsymbol{k} \to \boldsymbol{k} + e\boldsymbol{A}$ (where $e > 0$ is the electronic charge) with the vector potential $\boldsymbol{A} = -\int \boldsymbol{E}\, dt = -(E_0/\omega)(\sin\omega t \hat{x} - \mu\cos\omega t \hat{y})$. The total Hamiltonian then becomes $H = H_0 - (\Lambda/2)(\tau\sin\omega t \sigma_x - \mu\cos\omega t \sigma_y)$, where $\Lambda = 2eE_0 v/\omega$. The pump field couples to the orbital degrees of freedom only, and optical transitions preserve spins.

It will be convenient to define [38–40] a set of mutually perpendicular pseudospin unit vectors $\{\hat{\boldsymbol{\alpha}}_k, \hat{\boldsymbol{\beta}}_k, \hat{\boldsymbol{\gamma}}_k\}$ and corresponding basis matrices $(\sigma_\alpha, \sigma_\beta, \sigma_\gamma) = \boldsymbol{\sigma} \cdot (\hat{\boldsymbol{\alpha}}_k, \hat{\boldsymbol{\beta}}_k, \hat{\boldsymbol{\gamma}}_k)$ to rewrite the Hamiltonian. With the definition $\hat{\boldsymbol{k}}_\tau \equiv \cos\phi\hat{x} + \tau\sin\phi\hat{y}$, we define the unit vectors as

$$\hat{\boldsymbol{\alpha}}_k = \sin\theta_k \hat{\boldsymbol{k}}_\tau + \cos\theta_k \hat{z}, \quad (4)$$

$$\hat{\boldsymbol{\beta}}_k = \tau\hat{z} \times \hat{\boldsymbol{k}}_\tau, \quad (5)$$

$$\hat{\boldsymbol{\gamma}}_k = -\tau\cos\theta_k \hat{\boldsymbol{k}}_\tau + \tau\sin\theta_k \hat{z}. \quad (6)$$

$\{\hat{\boldsymbol{\alpha}}_k, \hat{\boldsymbol{\beta}}_k, \hat{\boldsymbol{\gamma}}_k\}$ forms a right-handed triad defined locally at each $\boldsymbol{k}$ point. Note that they are dependent on the valley index τ. $\{\sigma_\alpha, \sigma_\beta, \sigma_\gamma\}$ are the corresponding pseudospin projections

$$\sigma_\alpha = \begin{bmatrix} \cos\theta_k & \sin\theta_k e^{-i\tau\phi} \\ \sin\theta_k e^{i\tau\phi} & -\cos\theta_k \end{bmatrix}, \quad (7)$$

$$\sigma_\beta = i\tau\begin{bmatrix} 0 & -e^{-i\tau\phi} \\ e^{i\tau\phi} & 0 \end{bmatrix}, \quad (8)$$

$$\sigma_\gamma = \tau\begin{bmatrix} \sin\theta_k & -\cos\theta_k e^{-i\tau\phi} \\ -\cos\theta_k e^{i\tau\phi} & -\sin\theta_k \end{bmatrix}. \quad (9)$$

It is also useful to note that $\sigma_{\alpha,\beta,\gamma}$ is related to the usual Pauli matrices $\sigma_{x,y,z}$ through the pseudospin-to-band unitary transformation $\mathcal{U}_k \equiv [\chi_{k+}\, \chi_{k-}]$ by $\sigma_\alpha = \mathcal{U}_k\sigma_z\mathcal{U}_k^\dagger$, $\sigma_\beta = \mathcal{U}_k(\tau\sigma_y)\mathcal{U}_k^\dagger$, $\sigma_\gamma = \mathcal{U}_k(-\tau\sigma_x)\mathcal{U}_k^\dagger$. We can then represent the total Hamiltonian as follows:

$$H = \left[\alpha_k + \frac{\Lambda}{2}\mu\tau\sin\theta_k\sin(\phi - \mu\omega t)\right]\sigma_\alpha \quad (10)$$

$$+ \frac{\Lambda}{2}\mu\tau\cos(\phi - \mu\omega t)\sigma_\beta - \frac{\Lambda}{2}\mu\cos\theta_k\sin(\phi - \mu\omega t)\sigma_\gamma.$$

The total Hamiltonian above, now expressed in the new pseudospin representation, can be further transformed into the rotating frame using the unitary transformation $U = e^{-i\omega t\sigma_\alpha/2}$ as $\tilde{H} = U^\dagger H U - iU^\dagger \partial_t U$. Hereafter, quantities in the rotating frame (RF) will be denoted with an overhead tilde. In the RF-transformed pseudospin basis, σ_α is unchanged since it
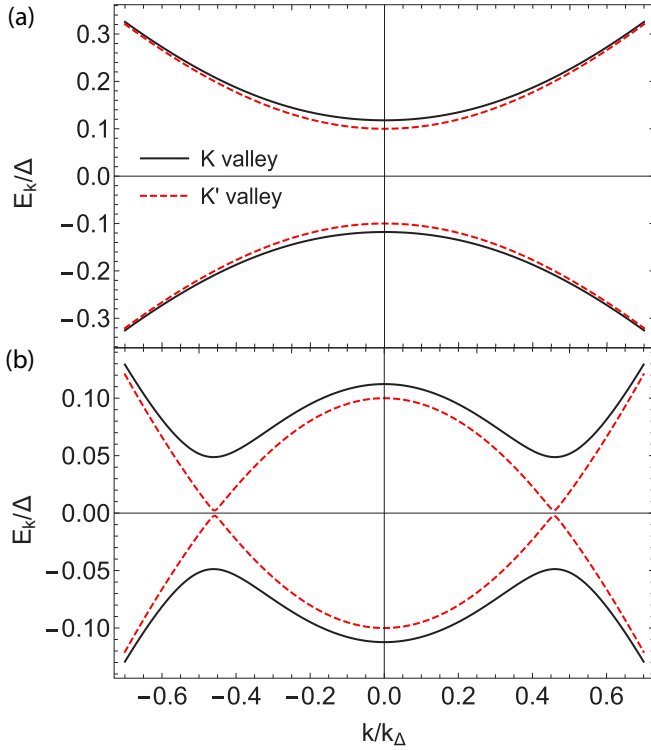
FIG. 1. Photon-dressed bands $\pm\tilde{E}_k$ for spin-up electrons at valley K (solid) and spin-down electrons at valley K' (dashed) under a circularly polarized pump field with strength $E_0 = 200$ MV/m and helicity $\mu = 1$. The equilibrium band-gap value is taken as $2\Delta = 2\Delta_1 = 1.585$ eV. Part (a) corresponds to subgap pump field frequency $\omega = 1.4$ eV, and (b) to above-gap frequency $\omega = 1.74$ eV. Energy values are scaled by Δ_1 and momentum k_x, k_y by $k_{\Delta_1} = \Delta_1/v$.

commutes with U, while the other two basis matrices become

$$U^{\dagger}\sigma_{\beta}U = \cos(\omega t)\sigma_{\beta} - \sin(\omega t)\sigma_{\gamma}, \quad (11)$$

$$U^{\dagger}\sigma_{\gamma}U = \cos(\omega t)\sigma_{\gamma} + \sin(\omega t)\sigma_{\beta}. \quad (12)$$

Following the rotating-wave approximation (RWA), we retain only time-independent terms and obtain the rotating-frame Hamiltonian as

$$\tilde{H} = \left(\alpha_k - \frac{\omega}{2}\right)\sigma_{\alpha} + \frac{\Lambda}{4}M_k(\cos\phi\,\sigma_{\beta} - \mu\sin\phi\,\sigma_{\gamma}), \quad (13)$$

where $M_k \equiv \mu\tau + \cos\theta_k$ captures the valley selection rule at $k = 0$ with $M_k = 2$ when $\mu = \tau$, and zero otherwise. Diagonalizing the Hamiltonian $\tilde{H}$ gives the photon-dressed conduction- and valence-band dispersions in the rotating frame,

$$\tilde{E}_k = \pm\sqrt{\left(\alpha_k - \frac{\omega}{2}\right)^2 + \left(\frac{\Lambda}{4}M_k\right)^2}. \quad (14)$$

Figure 1 shows the photon-dressed bands of the spin-up electrons at valley K and the spin-down electrons at valley K' for the cases when the light frequency is below and above the band gap. For circularly polarized light, the dispersion $\tilde{E}_k$ is isotropic in the k-space since M_k is independent of ϕ. For the case of subgap frequency $\omega < 2\Delta$ in Fig. 1(a), the band

gap is enhanced from the equilibrium value due to the dynamical Stark effect [41], becoming $\sqrt{\delta_d^2 + \Lambda^2}$ in the rotating frame, where $\delta_d = 2\Delta - \omega$ is the detuning. One notices that the difference between the photon-dressed bands at the two valleys is quite small even at large fields. A more dramatic difference can be seen when the frequency exceeds the band gap in Fig. 1(b). At both valleys, a dynamical gap is opened at a finite k value. The gap is sizable, ~77.2 meV, at valley K but is minuscule, ~3.7 meV, at valley K', which can be barely resolved at the scale of the plot.

The drastic difference between the two photon-dressed bands is a result of the valley-selective coupling of electrons with circularly polarized light through the matrix element M_k. From Eq. (14), the magnitude of the gap can be found as $\Lambda M_{k=k_r}/2$, where k_r is the momentum at which the resonance transition occurs when $2\alpha_{k_r} = \omega$. For frequency values near the TMD band gap such as $\omega = 1.7$ eV, to generate a dynamical gap of 10–100 meV at valley K, the range of ac field amplitude required is 25–250 MV/m, which is attainable in state-of-the-art ultrafast optical experiments [25,42,43]. In free-standing graphene, a strong circularly polarized light similarly opens up a dynamical gap at the Dirac points, and in recent experiments the induced Dirac gap is estimated to be ~70 meV [17].

The photon-dressed states Eq. (14), which are obtained within the RWA, capture similar physics to the Floquet states in the 2×2 truncated Floquet space in the neighborhood of a dynamical gap [44–46], with $\pm$ in Eq. (14) corresponding to the Floquet quasienergies of the zeroth conduction and first valence sidebands. For near-resonance frequencies $\omega \approx 2\Delta_1$ in TMDs, the dimensionless light-matter coupling parameter $\lambda = eE_0v/(\hbar\omega^2) \lesssim 10^{-2} \ll 1$ for E_0 up to 250 MV/m, therefore the system is well within the weak-coupling (also known as weak drive) regime in which the RWA is expected to provide an excellent approximation.

III. KINETIC EQUATION

To calculate the photocurrent response, we first obtain the density matrix ρ_k in the presence of the pump and probe fields. The Hamiltonian H including the pump field vector potential is treated as the nonperturbative part of the problem. The perturbative part is due to the weak dc probe field $\boldsymbol{E}$, which is included in the Hamiltonian in the form of a slowly varying scalar potential $\Phi(\boldsymbol{r})$ such that $e\boldsymbol{E} = \nabla\Phi(\boldsymbol{r})$. We follow the standard procedure to derive the equation of motion for the one-time density matrix using the nonequilibrium Green's function formalism [47,48]. After obtaining the quantum kinetic equation of the two-time lesser Green's function $G^<$, performing the Wigner transformation and gradient expansion, the equation of motion for the density matrix can be obtained from the kinetic equation of $G^<$ in the equal-time limit, which in frequency space translates to the following relation:

$$\rho_k(t) = -i\int_{-\infty}^{\infty}\frac{d\omega}{2\pi}G^<_{k,\omega}(t). \quad (15)$$

Performing the above steps, we then find the kinetic equation for ρ_k:

$$\frac{\partial \rho_k}{\partial t} - e\boldsymbol{E} \cdot \frac{\partial \rho_k}{\partial \boldsymbol{k}} + i[H, \rho_k] = I_s[\rho_k], \tag{16}$$

where H is the total Hamiltonian including the optical pump field in Sec. II, and $I_s[\rho_k]$ represents the scattering integral that describes the damping effects of relaxation and dephasing. Here intraband drift motion due to the dc field is included via the second term on the left-hand side of the kinetic equation. Since ρ_k is a 2×2 density matrix in the pseudospin space, it can be decomposed using the basis $\{\mathbb{I}, \sigma_\alpha, \sigma_\beta, \sigma_\gamma\}$ as

$$\rho_k = n_k \mathbb{I} + \tfrac{1}{2} \boldsymbol{S}_k \cdot \boldsymbol{\sigma}. \tag{17}$$

n_k and $\boldsymbol{S}_k$ have the meanings of a charge and a pseudospin distribution function, respectively. In this work, we confine ourselves to considering carrier scattering processes that are spin-conserving and valley-conserving. This assumption is valid when no magnetic impurity is present and atomic-scaled defects that give rise to intervalley scattering are negligible. Our approach here can be easily extended to include scattering that flips spins and valleys [49]. Then, in the relaxation-time approximation [41], the scattering integral takes the following form with phenomenological longitudinal relaxation rate Γ and transverse relaxation rate $\Gamma_\perp$:

$$I_s[\rho_k] = -\left[\Gamma\left(n_k - n_k^{(\mathrm{eq})}\right)\mathbb{I} + \frac{\Gamma}{2}\left(S_{k,\alpha} - S_{k,\alpha}^{(\mathrm{eq})}\right)\sigma_\alpha \right.$$
$$\left. + \frac{\Gamma_\perp}{2}S_{k,\beta}\sigma_\beta + \frac{\Gamma_\perp}{2}S_{k,\gamma}\sigma_\gamma \right], \tag{18}$$

where $S_{k,\alpha}, S_{k,\beta}, S_{k,\gamma}$ denote the components of $\boldsymbol{S}_k$ along $\{\hat{\boldsymbol{\alpha}}_k, \hat{\boldsymbol{\beta}}_k, \hat{\boldsymbol{\gamma}}_k\}$, respectively. $S_{k,\alpha}$ describes the population difference $S_{k,\alpha} = \rho_{k,cc} - \rho_{k,bb}$ between the conduction band (c) and the valence band (b) and is also known as interband population inversion (with $S_{k,\alpha} = 1$ for full inversion), whereas $S_{k,\beta}, S_{k,\gamma}$ describe interband coherence that leads to optical polarization. Γ and $\Gamma_\perp$ phenomenologically capture the effects of the decay of interband population inversion and optical polarization as well as intraband momentum relaxation. We note that inclusion of dissipative effects is essential for the irradiated system to attain the nonequilibrium steady state. Before light is turned on, the system is assumed to be in equilibrium and the Fermi level is inside the band gap, with a completely filled valence band and an empty conduction band so that $n_k^{(\mathrm{eq})} = 1/2$, $S_{k,\alpha}^{(\mathrm{eq})} = -1$, and $S_{k,\beta}^{(\mathrm{eq})} = S_{k,\gamma}^{(\mathrm{eq})} = 0$.

IV. EFFECTS OF PUMP FIELD: ZEROTH-ORDER DENSITY MATRIX

To obtain the photoconductivity, we solve Eq. (16) up to first order in $\boldsymbol{E}$ by linearizing the density matrix as $\rho_k = \rho_k^{(0)} + \rho_k^{(1)}$. The density matrix $\rho_k^{(0)}$ is the zeroth-order solution to Eq. (16) under a zero dc probe field $E = 0$, and $\rho_k^{(1)}$ is the first-order correction due to a finite E. Equation (16) then reduces to the following two equations satisfied by $\rho_k^{(0)}$ and $\rho_k^{(1)}$:

$$\frac{\partial \rho_k^{(0)}}{\partial t} + i[H, \rho_k^{(0)}] = I_s[\rho_k^{(0)}], \tag{19}$$

$$\frac{\partial \rho_k^{(1)}}{\partial t} - e\boldsymbol{E} \cdot \frac{\partial \rho_k^{(0)}}{\partial \boldsymbol{k}} + i[H, \rho_k^{(1)}] = I_s[\rho_k^{(1)}]. \tag{20}$$

Since we are interested in the steady-state regime, the above equations can be conveniently solved by transforming them into the rotating frame, in which the density matrix $\tilde{\rho}_k$ becomes time-independent within the RWA: $\partial \tilde{\rho}_k / \partial t = 0$. The resulting equations satisfied by $\tilde{\rho}_k^{(0)}$ and $\tilde{\rho}_k^{(1)}$ then take the same form as Eqs. (19) and (20) with $\partial / \partial t = 0$.

Our strategy for solving the 2×2 kinetic equation (19) in the pseudospin space is to project it onto the basis $\{\mathbb{I}, \sigma_\alpha, \sigma_\beta, \sigma_\gamma\}$, which produces four linearly independent equations that can be solved simultaneously. The zeroth- and first-order density matrices $\tilde{\rho}_k^{(0)}, \tilde{\rho}_k^{(1)}$ are then expanded, respectively, as

$$\tilde{\rho}_k^{(0,1)} = n_k^{(0,1)}\mathbb{I} + \tfrac{1}{2}\left(\tilde{S}_{k,\alpha}^{(0,1)}\sigma_\alpha + \tilde{S}_{k,\beta}^{(0,1)}\sigma_\beta + \tilde{S}_{k,\gamma}^{(0,1)}\sigma_\gamma\right). \tag{21}$$

The rotating frame Hamiltonian $\tilde{H}$, written in the new pseudospin basis, has been derived in Eq. (13). Since the set of basis matrices satisfy the usual commutation relation $[\sigma_i, \sigma_j] = 2i\epsilon_{ijk}\sigma_k$ with $i, j, k \in \{\alpha, \beta, \gamma\}$, one can easily find

$$\left[\tilde{H}, \tilde{\rho}_k^{(0)}\right] = \left(\alpha_k - \frac{\omega}{2}\right)\left(\tilde{S}_\beta^{(0)}i\sigma_\gamma - \tilde{S}_\gamma^{(0)}i\sigma_\beta\right)$$
$$- \frac{\Lambda}{4}M_k \cos\phi\left(\tilde{S}_\alpha^{(0)}i\sigma_\gamma - \tilde{S}_\gamma^{(0)}i\sigma_\alpha\right)$$
$$- \frac{\Lambda}{4}M_k\mu\sin\phi\left(\tilde{S}_\alpha^{(0)}i\sigma_\beta - \tilde{S}_\beta^{(0)}i\sigma_\alpha\right). \tag{22}$$

Note that the charge density distribution function n_k is decoupled from the kinetic equation for $\tilde{\boldsymbol{S}}_k$ since the contribution from n_k vanishes in Eq. (22) upon commutation operation. Substituting Eqs. (21) and (22) into the kinetic equation and solving, we find the steady-state solution for $\tilde{\rho}_k^{(0)}$:

$$\tilde{\rho}_k^{(0)} = n_k^{(\mathrm{eq})}\mathbb{I} + \tfrac{1}{2}S_{k,0}\sigma_\alpha + \tfrac{1}{2}(S_{k,1}\cos\phi + S_{k,2}\sin\phi)\sigma_\beta$$
$$+ \tfrac{1}{2}\mu(S_{k,2}\cos\phi - S_{k,1}\sin\phi)\sigma_\gamma, \tag{23}$$

where

$$\begin{bmatrix} S_{k,0} \\ S_{k,1} \\ S_{k,2} \end{bmatrix} = \frac{-1}{(2\alpha_k - \omega)^2 + \Gamma_\perp^2 + (\Lambda M_k/2)^2\Gamma_\perp/\Gamma}$$
$$\times \begin{bmatrix} (2\alpha_k - \omega)^2 + \Gamma_\perp^2 \\ (\Lambda M_k/2)(2\alpha_k - \omega) \\ -(\Lambda M_k/2)\mu\Gamma_\perp \end{bmatrix}. \tag{24}$$

Figures 2(a)–2(d) show the interband population difference $\tilde{S}_{k,\alpha}^{(0)} = S_{k,0}$ at valleys K and K' under a circularly polarized pump field with helicity $\mu = 1$ for the cases when the frequency is below and above the band gap. When $\omega < 2\Delta$ [Figs. 2(a) and 2(b)], a small population of electrons is excited into the conduction band localized around the band edge $k = 0$. Most of the electron population remains in the valence band, with $\tilde{S}_{k,\alpha}^{(0)} \approx -1$. For $\omega > 2\Delta$ [Figs. 2(c) and 2(d)], electrons of both valleys are excited predominantly to those states that are peripheral to the ring of resonant states $\omega = 2\alpha_k$ where the dynamical gap opens [Fig. 1(b)]. Near those states around the circular "opening" in Fig. 2(c) for valley K, $\tilde{S}_{k,\alpha}^{(0)}$ reaches a maximum of $\sim -10^{-4}$ indicating that
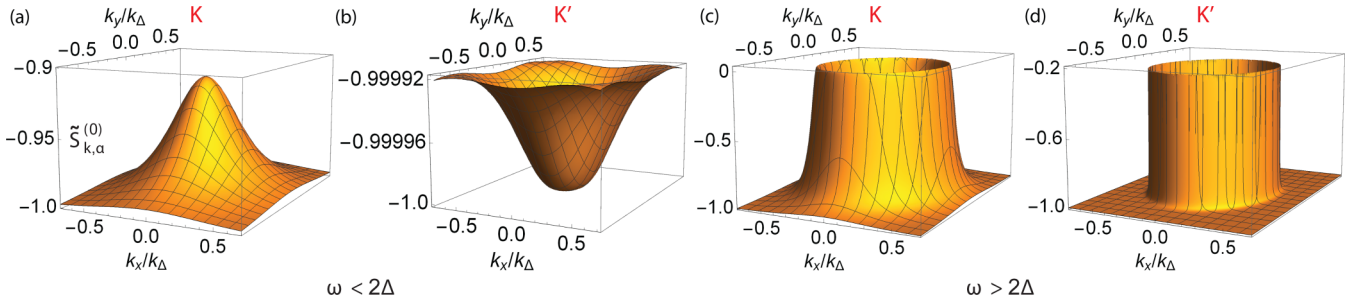
FIG. 2. Population difference $\tilde{S}_{k,\alpha}^{(0)} = S_{k,0}$ between the conduction and valence bands at valley K and K' under a circularly polarized pump field with helicity $\mu = 1$ and strength $E_0 = 100$ MV/m for (a),(b) $\omega = 1.4$ eV and (c),(d) $\omega = 1.74$ eV. The labels for the K and K' valleys are indicated above the plots. Relaxation and dephasing parameters are taken as $\Gamma = \Gamma_\perp = 1$ meV, and the equilibrium band gap 2Δ is the same as in Fig. 1. Note the difference in scales in the plots (a) and (b).

the valence-band electrons there are strongly excited to the conduction band. In comparison, fewer electrons are photoexcited at valley K' as shown in Fig. 2(d), where the maximum $\tilde{S}_{k,\alpha}^{(0)}$ reaches about -0.3. Because the dynamical gap is much smaller at K' than at K [Fig. 1(b)], the excited populations at K' are localized closely at the resonant states resulting in a much sharper distribution of $\tilde{S}_{k,\alpha}^{(0)}$ in the momentum space.

V. EFFECTS OF dc BIAS: FIRST-ORDER DENSITY MATRIX

Having obtained the steady-state solution to Eq. (19), we proceed to solve Eq. (20) in the rotating frame using the decomposition Eq. (21) for $\tilde{\rho}_k^{(1)}$. The dc electric field is taken as $\boldsymbol{E} = E\hat{x}$ directed along $\hat{x}$. The $\boldsymbol{E}$-dependent driving term in Eq. (20) is completely determined by $\tilde{\rho}_k^{(0)}$ and can be resolved as

$$e\boldsymbol{E} \cdot \frac{\partial \tilde{\rho}_k^{(0)}}{\partial \boldsymbol{k}} = eE(\mathcal{D}_{\mathbb{I}}\mathbb{I} + \mathcal{D}_{k,\alpha}\sigma_\alpha + \mathcal{D}_{k,\beta}\sigma_\beta + \mathcal{D}_{k,\gamma}\sigma_\gamma), \quad (25)$$

with functions $\mathcal{D}_{\mathbb{I}}, \mathcal{D}_{k,\alpha}, \mathcal{D}_{k,\beta}, \mathcal{D}_{k,\gamma}$ as coefficients. From Eqs. (23) and (24) it is obvious that $\mathcal{D}_{\mathbb{I}} = 0$, and we can obtain explicit expressions of $\mathcal{D}_{k,\alpha}, \mathcal{D}_{k,\beta}, \mathcal{D}_{k,\gamma}$ as provided in Appendix A. The commutator $[\tilde{H}, \tilde{\rho}_k^{(1)}]$ is the same as in Eq. (22) with the superscript (0) replaced by (1). It follows that $n_k^{(1)} = 0$ and $\tilde{S}_{k,\alpha}^{(1)}, \tilde{S}_{k,\beta}^{(1)}, \tilde{S}_{k,\gamma}^{(1)}$ are determined by

$$\begin{bmatrix} \Gamma & -\frac{\Delta}{2}M_k\mu\sin\phi & -\frac{\Delta}{2}M_k\cos\phi \\ \frac{\Delta}{2}M_k\mu\sin\phi & \Gamma_\perp & (2\alpha_k - \omega) \\ \frac{\Delta}{2}M_k\cos\phi & -(2\alpha_k - \omega) & \Gamma_\perp \end{bmatrix} \begin{bmatrix} \tilde{S}_{k,\alpha}^{(1)} \\ \tilde{S}_{k,\beta}^{(1)} \\ \tilde{S}_{k,\gamma}^{(1)} \end{bmatrix}$$
$$= 2eE \begin{bmatrix} \mathcal{D}_{k,\alpha} \\ \mathcal{D}_{k,\beta} \\ \mathcal{D}_{k,\gamma} \end{bmatrix}. \quad (26)$$

The above equation gives explicit analytic expressions for $\tilde{S}_{k,\alpha}^{(1)}, \tilde{S}_{k,\beta}^{(1)}, \tilde{S}_{k,\gamma}^{(1)}$, which are relegated in Appendix B. In Figs. 3(a)–3(d), we show the correction to the population difference $\tilde{S}_{k,\alpha}^{(1)}$ due to the dc electric field at both valleys for the ω below and above the band gap. Since $\tilde{S}_{k,\alpha}^{(1)}$ is proportional to E, we plot $\tilde{S}_{k,\alpha}^{(1)}/E$. In contrast to $\tilde{S}_{k,\alpha}^{(0)}$, $\tilde{S}_{k,\alpha}^{(1)}$ is asymmetric in k-space due to the dc field breaking in-plane rotational symmetry. Below the band gap [Figs. 3(a) and 3(b)], $\tilde{S}_{k,\alpha}^{(1)}$ is generally very small. For a dc field $E = 10$ kV/m, for

instance, $\tilde{S}_{k,\alpha}^{(1)} \sim 10^{-4}$ at valley K and $\tilde{S}_{k,\alpha}^{(1)} \sim 10^{-7}$ at valley K'. When the frequency is increased to above the band gap, $\tilde{S}_{k,\alpha}^{(1)}$ is dramatically enhanced near the resonant states by two and six orders of magnitude, respectively, as seen in Figs. 3(c) and 3(d). This shows that a resonant pump field excitation induces a much stronger effect on the photoexcited population distribution perturbed by the dc bias.

The degree of asymmetry can be analyzed by resolving $\tilde{S}_{k,\alpha}^{(1)}$ into even and odd harmonics of ϕ. While Figs. 3(a) and 3(d) seem to show only an asymmetry along the k_x direction, there is also a small degree of asymmetry along the k_y direction that is not apparent at the scale of the plots. In Appendix B we show the explicit expressions of the first odd ($\sin\phi$) and even ($\cos\phi$) harmonics of $\tilde{S}_{k,\alpha}^{(1)}$, which corresponds to asymmetries along the k_y and k_x directions, respectively. As we will explain in Sec. VI, the asymmetry of this distribution function along the transverse direction to the dc bias, along with smaller effects from the interband responses $\tilde{S}_{k,\beta}^{(1)}$ and $\tilde{S}_{k,\gamma}^{(1)}$, leads to the photoinduced anomalous Hall effect.

The preferential coupling between the left (right) circularly polarized light and the K (K') valley results in a population imbalance of photoexcited conduction-band electrons between the two valleys. Using the pseudospin-to-band unitary transformation $\mathcal{U}_k$, the conduction-band density matrix can be found as $\rho_{k,cc} = n_k + \tilde{S}_{k,\alpha}/2$. $\rho_{k,cc}$ is predominantly given by the zeroth-order contribution $n_k^{(eq)} + S_{k,0}/2$ as the correction $\tilde{S}_{k,\alpha}^{(1)}/2$ induced by the dc bias is comparatively small. Because $n_k^{(eq)} = 1/2$ is independent of the valley degrees of freedom, the conduction-band population difference between the two valleys is $\Delta n_v = \sum_k (\rho_{k,cc}^K - \rho_{k,cc}^{K'}) = \sum_k [(S_{k,0} + \tilde{S}_{k,\alpha}^{(1)})^K - (S_{k,0} + \tilde{S}_{k,\alpha}^{(1)})^{K'}]/2$. Then the total population imbalance can be found by summing over the spin degrees of freedom in the original TMD Hamiltonian Eq. (1), which correspond to the two values of the gap $2\Delta_1$ and $2\Delta_2$. They give the interband transition energies at $k = 0$ for the two spins. Figure 4 shows the resulting total Δn_v as a function of the frequency for different values of the pump field. Although the RWA is valid for frequencies near the band edges, for display purposes we show an extended range of ω in Figs. 4 and 5. Near the band edges, Δn_v exhibits a shoulderlike feature when the frequency reaches $2\Delta_1$ and then peaks at the second gap $2\Delta_2$. Away from the band edges, Δn_v gradually tails off toward higher frequencies, while it approaches zero toward lower frequencies inside the band gap.
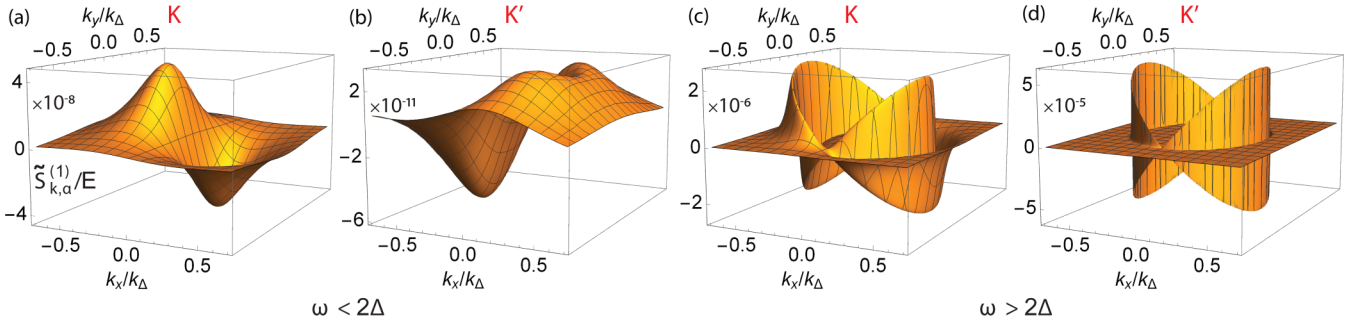
FIG. 3. First-order correction to the population difference $\tilde{S}_{k,\alpha}^{(1)}/E$ scaled by the dc bias field E between the conduction and valence bands at valley K and K' for (a),(b) $\omega = 1.4$ eV and (c),(d) $\omega = 1.74$ eV. The labels for the K and K' valleys are indicated above the plots. The pump field has the same helicity and strength, and the values of Γ, $\Gamma_\perp$, Δ are the same as in Fig. 2.

We note that the latter two trends could in principle receive a small non-RWA correction not captured in our theory as the frequency is tuned further away from the band edges. At this point, it may be tempting to obtain the anomalous Hall conductivity from this valley population imbalance as in the dc case. However, because of the formation of photon-dressed bands in the presence of a pump field, the photoinduced Hall current is no longer simply given by this valley population imbalance and the Berry curvatures of the equilibrium bands. We can estimate the Hall conductivity obtained in this way [15] using Fig. 4, and we find that it is an order of magnitude too small compared to our exact results presented in Fig. 5. Instead, the photoinduced transport currents are determined by the distribution function $\tilde{S}_k^{(1)}$ of the photon-dressed bands as described below.

VI. LONGITUDINAL AND ANOMALOUS HALL PHOTOCONDUCTIVITIES

To calculate the photovoltaic current, the density matrix needs to be transformed back into the stationary frame $\rho_k^{(1)} = U\tilde{\rho}_k^{(1)}U^\dagger$,

$$\rho_k^{(1)} = n_k^{(1)}\mathbb{I} + \frac{1}{2}\tilde{S}_{k,\alpha}^{(1)}\sigma_\alpha + \frac{1}{2}\left(\tilde{S}_{k,\beta}^{(1)}\cos\omega t - \tilde{S}_{k,\gamma}^{(1)}\sin\omega t\right)\sigma_\beta$$
$$+ \frac{1}{2}\left(\tilde{S}_{k,\beta}^{(1)}\sin\omega t + \tilde{S}_{k,\gamma}^{(1)}\cos\omega t\right)\sigma_\gamma. \quad (27)$$
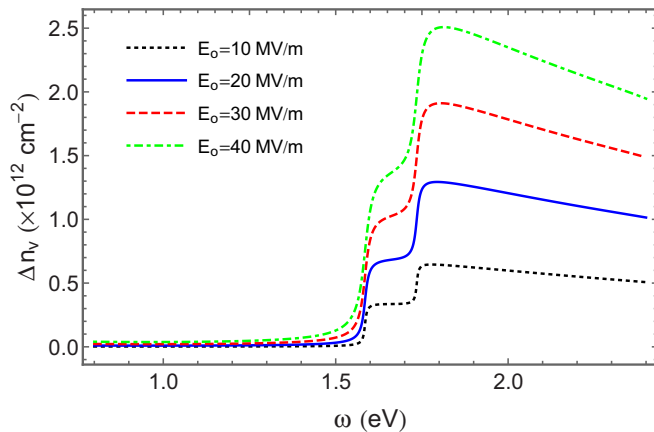

FIG. 4. Conduction-band population difference between the two valleys to the zeroth order, as a function of ω for different values of E_0 with $\mu = 1$. Relaxation and dephasing parameters are taken as $\Gamma = \Gamma_\perp = 1$ meV.

The expectation value of the current density is then calculated from $\boldsymbol{J} = \Sigma_k \text{Tr}\{\boldsymbol{j}_k(t)\rho_k^{(1)}(t)\}$, where "Tr" denotes trace over degrees of freedom other than the momentum, and $\boldsymbol{j}_k(t)$ is the single-electron current operator,

$$\boldsymbol{j}_k(t) = -e\frac{\partial H_R(t)}{\partial \boldsymbol{k}} = -e\left(\frac{\partial H_R}{\partial k}\hat{\boldsymbol{k}} + \frac{1}{k}\frac{\partial H_R}{\partial \phi}\hat{\boldsymbol{\phi}}\right). \quad (28)$$

$H_R(t)$ above is the stationary-frame Hamiltonian *within the RWA*, and it can be obtained by transforming $\tilde{H}$ in Sec. II back to the stationary frame $H_R(t) = U\tilde{H}U^\dagger - iU\partial_t U^\dagger$,

$$H_R(t) = \alpha_k\sigma_\alpha + \frac{\Lambda}{4}M_k(\cos\phi\cos\omega t + \mu\sin\phi\sin\omega t)\sigma_\beta$$
$$+ \frac{\Lambda}{4}M_k(\cos\phi\sin\omega t - \mu\sin\phi\cos\omega t)\sigma_\gamma. \quad (29)$$

The matrix trace calculation can be facilitated by decomposing the longitudinal (x-direction) and transverse (y-direction) single-electron current operators into components of $\{\sigma_\alpha, \sigma_\beta, \sigma_\gamma\}$, such that $j_i(t) = \hat{\boldsymbol{i}} \cdot \boldsymbol{j}_k(t) = j_{i,\alpha}(t)\sigma_\alpha + j_{i,\beta}(t)\sigma_\beta + j_{i,\gamma}(t)\sigma_\gamma$ with $i \in \{x, y\}$. Explicit expressions of $j_{i,\alpha}(t)$, $j_{i,\beta}(t)$, $j_{i,\gamma}(t)$ are relegated to Appendix A. It is easy to verify that the basis matrices satisfy the trace relation $\text{Tr}\{\sigma_\mu\sigma_\nu\} = 2\delta_{\mu\nu}$, where $\mu, \nu \in \{\alpha, \beta, \gamma\}$. Using this property with Eq. (27), the photovoltaic longitudinal and Hall currents can be calculated from $\rho_k^{(1)}$ as

$$J_i = \sum_k \left[\tilde{S}_{k,\alpha}^{(1)}j_{i,\alpha} + \left(\tilde{S}_{k,\beta}^{(1)}\cos\omega t - \tilde{S}_{k,\gamma}^{(1)}\sin\omega t\right)j_{i,\beta}\right.$$
$$\left. + \left(\tilde{S}_{k,\beta}^{(1)}\sin\omega t + \tilde{S}_{k,\gamma}^{(1)}\cos\omega t\right)j_{i,\gamma}\right]. \quad (30)$$

Before proceeding to calculate the photoconductivities, it is useful to first check that our formulation recovers the correct dark conductivity. The scenario of vanishing pump field corresponds to taking the limit $\Lambda, \omega \to 0$ such that $\Lambda/\omega \to 0$. The rotating frame reduces to the stationary frame, and the Hamiltonian in Eq. (13) becomes the original Hamiltonian without light, $H = \alpha_k\sigma_\alpha$. Damping terms Γ, $\Gamma_\perp$ can be taken as zero because the Fermi energy lies within the band gap. Solutions to Eq. (26) then reduce to

$$\tilde{S}_{k,\alpha}^{(1)} = 0, \quad (31)$$

$$\tilde{S}_{k,\beta}^{(1)} = -\frac{\tau eE}{2k\alpha_k}\sin\theta_k\cos\theta_k\cos\phi, \quad (32)$$

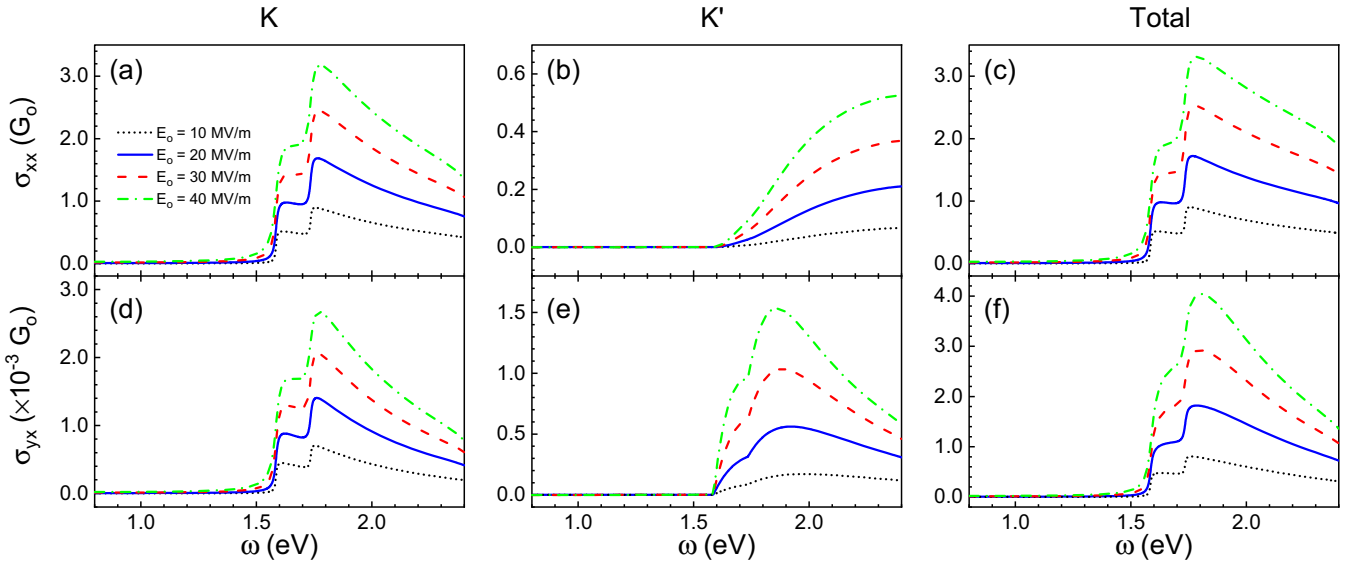$$\tilde{S}_{k,\gamma}^{(1)} = \frac{eE}{2k\alpha_k}\sin\theta_k\sin\phi. \quad (33)$$

FIG. 5. Longitudinal σ_{xx} and Hall σ_{yx} conductivities in units of $G_0 = e^2/\hbar$ as a function of ω under different strengths of pump field E_0 with helicity $\mu = 1$. Panels (a) and (d) show the contributions due to the K valley ($\tau = 1$), while (b) and (e) show the K' valley ($\tau = -1$), and panels (c) and (f) show the sum of the two valleys' contributions. Relaxation and dephasing rates are the same as in Fig. 4.

From Eq. (27), the first-order density matrix then becomes

$$\rho_k^{(1)} = n_k^{(1)}\mathbb{I} - \frac{\tau e E}{4 k \alpha_k}\sin\theta_k(\cos\theta_k\cos\phi\sigma_\beta - \tau\sin\phi\sigma_\gamma). \quad (34)$$

The y-component of the single-electron current operator in Eq. (28) reduces to $-ev\sigma_y$, which when written in a pseudospin basis is

$$j_y = -e\frac{\alpha_k\sin\theta_k}{k}(\sin\theta_k\sin\phi\sigma_\alpha + \cos\phi\sigma_\beta$$
$$-\tau\cos\theta_k\sin\phi\sigma_\gamma). \quad (35)$$

Calculating the transverse current $J_y = \Sigma_k\mathrm{Tr}\{j_y\rho_k^{(1)}\}$, we recover the well-known dark valley-resolved Hall conductivity $\sigma_{yx}^\tau = J_y/E = \tau e^2/4\pi\hbar$ where the superscript τ distinguishes the contribution from each valley. Similarly, we find a vanishing longitudinal conductivity $\sigma_{xx}^\tau = 0$ for a vanishing pump field, as expected for undoped TMDs.

We now return to Eq. (30). Subtracting off the dark current contribution and integrating over one time period, we obtain the following expressions for the time-averaged photoinduced longitudinal and Hall currents for spin s and valley τ:

$$J_x = \sum_k \frac{\sin^2\theta_k}{k}\left\{\tilde{S}_{k,\alpha}^{(1)}\alpha_k\cos\phi + \frac{\mu\Lambda}{8}\tilde{S}_{k,\gamma}^{(1)}M_{k,+}\sin 2\phi\right.$$
$$\left. + \frac{\Lambda}{8}\tilde{S}_{k,\beta}^{(1)}[M_{k,-} - M_{k,+}\cos 2\phi]\right\}, \quad (36)$$

$$J_y = \sum_k \frac{\sin^2\theta_k}{k}\left\{\tilde{S}_{k,\alpha}^{(1)}\alpha_k\sin\phi - \frac{\Lambda}{8}\tilde{S}_{k,\beta}^{(1)}M_{k,+}\sin 2\phi\right.$$
$$\left. - \frac{\mu\Lambda}{8}\tilde{S}_{k,\gamma}^{(1)}[M_{k,-} + M_{k,+}\cos 2\phi]\right\}, \quad (37)$$

where $M_{k,\pm} = \mu\tau \pm \cos\theta$. In Eqs. (36) and (37), the first term dependent on $\tilde{S}_{k,\alpha}^{(1)}$ corresponds to a Drude-like intraband response to the dc bias from the photon-dressed conduction and

valance bands, whereas the second and third terms dependent on $\tilde{S}_{k,\beta}^{(1)}$, $\tilde{S}_{k,\gamma}^{(1)}$ arise from interband response to the dc bias. Because of the momentum integration, it is clear that only the first odd (even) harmonic of $\tilde{S}_{k,\alpha}^{(1)}$ contributes to the intraband response of J_y (J_x), while only the zeroth, second odd and even harmonics of $\tilde{S}_{k,\beta}^{(1)}$, $\tilde{S}_{k,\gamma}^{(1)}$ enter into the interband responses of J_y and J_x. The total longitudinal and Hall photoconductivities are finally obtained by summing Eqs. (36) and (37) over the spin and valley degrees of freedom and dividing over the dc probe field E. In the dc anomalous Hall effect, interband coherences give rise to the intrinsic geometric contribution in ferromagnetic metals and in particular to a quantized topological contribution in magnetic insulators [50,51].

Figure 5 shows our numerical results for the valley-specific and total photoconductivities under left circularly polarized light ($\mu = 1$) calculated from Eqs. (36) and (37). One first notices that the K valley contribution is larger than that of the K' valley for both the longitudinal [Figs. 5(a) and 5(b)] and Hall conductivities [Figs. 5(d) and 5(e)]. Similar to Δn_v, the shoulder and peak features at $\omega = 2\Delta_1$ and $2\Delta_2$ are clearly visible for σ_{xx} and σ_{yx} at valley K, while they are less prominent for the conductivities at valley K'. Interestingly, we find that the photoinduced σ_{yx} at the two valleys carry the same sign, in contrast to the unpumped case, in which different valley contributions to the dark Hall conductivity have opposite signs. The underlying reason can be seen as follows.

In Eq. (37) for the Hall conductivity, the contributions from interband responses $\tilde{S}_{k,\beta}^{(1)}$, $\tilde{S}_{k,\gamma}^{(1)}$ are typically small compared to the contribution due to population inversion $\tilde{S}_{k,\alpha}^{(1)}$, as shown in Appendix C. Moreover, these interband response terms are dominated by their K valley contributions, which are larger than the corresponding K' contributions by two orders of magnitude. Therefore, the valley dependence of σ_{yx} is principally due to the intraband response term from $\tilde{S}_{k,\alpha}^{(1)}$. Figures 6(a) and 6(b) show an intensity plot of the first odd
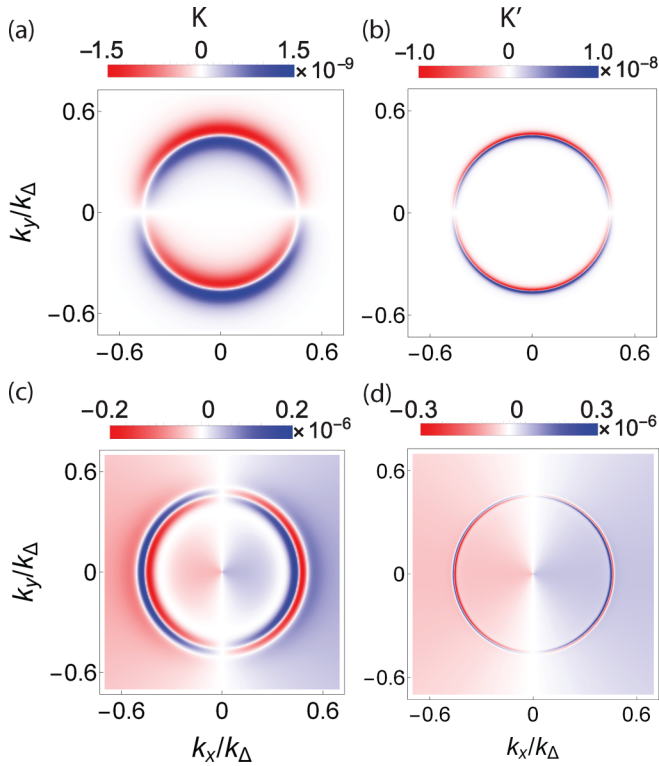
FIG. 6. First harmonic components of $\tilde{S}_{k,\alpha}^{(1)}/E$ at $E_0 = 100$ MV/m, $\omega = 1.74$ eV, and helicity $\mu = 1$. The $\sin\phi$ component is shown in (a) for valley K and (b) for valley K', while the $\cos\phi$ component is shown in (c) for valley K and (d) for valley K'. Relaxation and dephasing rates are taken as $\Gamma = \Gamma_\perp = 7$ meV.

harmonic component of $\tilde{S}_{k,\alpha}^{(1)}$ that contributes to the Hall conductivity through Eq. (37). One can see that $\tilde{S}_{k,\alpha}^{(1)}$ at valleys K and K' [panels (a) and (b)] share the same sign as indicated by the same color at every k-point, and thus contribute to the photoinduced Hall current with the same sign. In the case of the longitudinal conductivity in Eq. (36), we find that the intraband contribution dominates over the contributions from interband responses, so σ_{xx} is largely contributed by the $\cos\phi$ harmonic component of $\tilde{S}_{k,\alpha}^{(1)}$. As shown in Figs. 6(c) and 6(d), the first even harmonic also shares the same sign between the two valleys but is generally much larger than the first odd harmonic.

The origin of the first odd harmonic in $\tilde{S}_{k,\alpha}^{(1)}$ arises from terms with a $(\boldsymbol{E} \times \boldsymbol{k})_z$ dependence in the driving term of the kinetic equation (25) [which results in terms $\propto S_{k1,2}M_{k,-}/k$ in Eqs. (A2) and (A3)]. These terms originate from interband coherences $S_{k,1}$ and $S_{k,2}$ in the photon-dressed bands [Eqs. (23) and (24)] and vanish when the pump field goes to zero, therefore they are purely induced by the dressing photon field. Thus, we can distinguish two types of interband coherence effects: one that is primarily induced by the dc bias, and one that is primarily induced by the pump field. When there is no irradiation, the dark Hall conductivity is only due to the interband coherence originating from the off-diagonal elements of $\tilde{S}_k^{(1)}$, the interband response to the dc bias. Under irradiation, however, the photon-dressed conduction and valence bands are coherent mixtures of the equilibrium conduction

and valence bands hybridized by the one-photon excitation process. This photon-induced interband coherence therefore also enters into the intraband response $\tilde{S}_k^{(1)}$ under a dc bias, and it plays a more dominant role than the interband responses $\tilde{S}_{k,\beta}^{(1)}, \tilde{S}_{k,\gamma}^{(1)}$.

Returning to Fig. 5, panels (c) and (f) show the total conductivities obtained from summing the two valleys' contributions. The magnitude of σ_{xx} is about three orders of magnitude larger than that of σ_{yx}. If the circular polarization state is changed from $\mu = 1$ to -1, our numerical results show that both the magnitude and sign of the longitudinal conductivity remain unchanged, while the valley-specific contributions of the Hall conductivity are changed according to $\sigma_{yx}^{\tau=\mp 1,\mu=-1} = -\sigma_{yx}^{\tau=\pm 1,\mu=1}$, resulting in an overall sign change of the total Hall conductivity σ_{yx} as expected on the grounds of time-reversal.

To summarize, we find that both the photoinduced anomalous Hall and longitudinal conductivities are chiefly due to the intraband response of photon-dressed electrons arising from their asymmetric momentum-space distribution functions, which can be attributed to interband coherences directly induced by the pump field. This is accompanied by generally smaller contributions due to interband coherence effects induced by the dc bias. The latter, which correspond to the off-diagonal elements of the density matrix in the band representation, are the origin of geometric effects and give rise to Berry curvatures [52–54]. Hence our findings imply that the intrinsic geometric response to the dc field only plays a secondary role in the photoinduced anomalous Hall effect, in contrast to the case of the dc valley Hall effect [4,6]. Our findings here are consistent with Ref. [18], which reached a similar conclusion for photoexcited graphene.

In this work, we have provided a noninteracting theory for the photoinduced anomalous Hall effect, neglecting the effects of excitons and trions. This is justified because excitons under a dc bias are rapidly dissociated into free electrons and holes [55,56] that contribute to steady-state transport. Trion effects, on the other hand, do not contribute in the undoped samples we are considering where the equilibrium Fermi level lies deep within the band gap. Excitonic effects, however, could contribute in a more subtle way. In systems whose low-energy Hamiltonian breaks Galilean invariance, excitonic effects couple the intraband and interband dynamics resulting in interaction-induced correction in dynamic transport properties such as the Drude weight [57,58]. This effect is strongest in gapless systems such as graphene and is generally suppressed with an increasing band gap [59]. Although TMDs have a large band gap, their electron-electron interaction effect is also stronger than in graphene or gapped bilayer graphene, and further study could shed light on whether the competition between these two effects would lead to considerable interaction correction to the anomalous Hall conductivity. In this paper, we have considered only the intrinsic band-structure contribution to the photoinduced anomalous Hall effect. A further extension of our theory could include the extrinsic effect due to spin-orbit scattering with impurities [50], which will be a subject of future investigation. Finally, we emphasize that while we are motivated by TMDs in this work, the theoretical method we developed for the massive Dirac model

and its massless limit can be applied more generally to other materials with gapped or gapless Dirac quasiparticles [60–62] driven by a strong pump field.

VII. CONCLUSION

To close, we have presented a theory for the photoinduced valley Hall transport for undoped 2D transition-metal dichalcogenides under a strong optical pump field. Our theory is developed using the density matrix formalism, which enables treatment of the photon-dressed bands and carrier kinetics on an equal footing. The conceptual simplicity of our method allows us to obtain useful theoretical insights on the population distribution of the photon-dressed bands. Under a circularly polarized pump field, we find considerable differences in the photon-dressed bands and the nonequilibrium carrier distributions at the two valleys due to the valley-dependent optical selection rule. In each valley, electrons are predominantly excited to photon-dressed states around the dynamical gap. Both the valley polarization and the pho-

toinduced anomalous Hall conductivity are found to increase with the pump field and display notable signatures at the spin-resolved interband (i.e., "A" and "B") transition energies. Despite this similarity, we show that valley polarization plays a less important role in causing the photoinduced Hall effect than was commonly assumed, and the Hall effect is mainly driven by an asymmetric momentum-space distribution of photon-dressed electrons in the transverse direction. The theory and findings presented in this work highlight the important role of photon-dressed bands in understanding photoinduced transport, and they demonstrate the viability of optical control of spins and valleys through the photon-dressing effects of electronic bands.

APPENDIX A: DRIVING TERM $\mathcal{D}$ AND SINGLE-PARTICLE CURRENT OPERATORS j_x AND j_y

In this Appendix, we provide explicit analytic expressions for the quantities that are too lengthy to be included in the main text. By decomposing the driving term in the kinetic equation as in Eq. (25) into the identity and transformed Pauli matrices, we have

$$\mathcal{D}_{k,\alpha} = \frac{1}{2}\left\{\cos\phi\left[\frac{\partial S_{k0}}{\partial k} + \mu\tau\frac{\partial\theta_k}{\partial k}(S_{k2}\cos\phi - S_{k1}\sin\phi)\right] + \frac{1}{k}\sin\phi\sin\theta(S_{k1}\cos\phi + S_{k2}\sin\phi)\right\}, \tag{A1}$$

$$\mathcal{D}_{k,\beta} = \frac{1}{2}\left\{\cos\phi\left(\frac{\partial S_{k1}}{\partial k}\cos\phi + \frac{\partial S_{k2}}{\partial k}\sin\phi\right) - \frac{1}{k}\sin\phi[\sin\theta S_{k0} - \mu\tau(S_{k1}\sin\phi - S_{k2}\cos\phi)M_{k,-}]\right\}, \tag{A2}$$

$$\mathcal{D}_{k,\gamma} = \frac{1}{2}\left\{\cos\phi\left[\mu\left(\frac{\partial S_{k2}}{\partial k}\cos\phi - \frac{\partial S_{k1}}{\partial k}\sin\phi\right) - S_{k0}\tau\frac{\partial\theta_k}{\partial k}\right] + \frac{1}{k}\tau\sin\phi(S_{k1}\cos\phi + S_{k2}\sin\phi)M_{k,-}\right\}. \tag{A3}$$

The single-particle current operator is calculated in the stationary frame from the Hamiltonian in Eq. (29) obtained within the RWA,

$$j_{x,\alpha} = -e\left[\frac{\partial\alpha_k}{\partial k}\cos\phi + \frac{\Lambda}{8}(M_{k,+})^2\frac{1}{k}\tau\sin\theta\sin\omega t + \frac{\Lambda}{8}\frac{1}{k}\tau\sin^3\theta(-\sin\omega t\cos 2\phi + \mu\sin 2\phi\cos\omega t)\right], \tag{A4}$$

$$j_{x,\beta} = -e\left[-\alpha_k\sin\theta\frac{1}{k}\sin\phi + \frac{\Lambda}{8}\frac{1}{k}\sin^2\theta M_{k,-}\cos\omega t - \frac{\Lambda}{8}\frac{1}{k}\sin^2\theta M_{k,+}(\cos\omega t\cos 2\phi + \mu\sin 2\phi\sin\omega t)\right], \tag{A5}$$

$$j_{x,\gamma} = -e\left[-\tau\alpha_k\sin\theta\cos\theta\frac{1}{k}\cos\phi + \frac{\Lambda}{8}\frac{1}{k}\sin^2\theta M_{k,-}\sin\omega t + \frac{\Lambda}{8}\frac{1}{k}\sin^2\theta M_{k,+}(\mu\cos\omega t\sin 2\phi - \cos 2\phi\sin\omega t)\right]. \tag{A6}$$

$$j_{y,\alpha} = -e\left[\frac{\partial\alpha_k}{\partial k}\sin\phi - \frac{\Lambda}{8}(M_{k,+})^2\frac{1}{k}\mu\tau\sin\theta\cos\omega t - \frac{\Lambda}{8}\frac{1}{k}\tau\sin^3\theta(\sin\omega t\sin 2\phi + \mu\cos 2\phi\cos\omega t)\right], \tag{A7}$$

$$j_{y,\beta} = -e\left[\alpha_k\sin\theta\frac{1}{k}\cos\phi + \frac{\Lambda}{8}\frac{1}{k}\mu\sin^2\theta M_{k,-}\sin\omega t + \frac{\Lambda}{8}\frac{1}{k}\sin^2\theta M_{k,+}(-\cos\omega t\sin 2\phi + \mu\cos 2\phi\sin\omega t)\right], \tag{A8}$$

$$j_{y,\gamma} = -e\left[-\tau\alpha_k\sin\theta\cos\theta\frac{1}{k}\sin\phi - \frac{\Lambda}{8}\mu\frac{1}{k}\sin^2\theta M_{k,-}\cos\omega t - \frac{\Lambda}{8}\frac{1}{k}\sin^2\theta M_{k,+}(\mu\cos\omega t\cos 2\phi + \sin 2\phi\sin\omega t)\right]. \tag{A9}$$

APPENDIX B: FIRST-ORDER DENSITY MATRIX

The solutions obtained by solving Eq. (26) are presented as follows. First, in the current expressions Eqs. (36) and (37), we observe the following ϕ-dependence: $\tilde{S}_{k,\alpha}^{(1)}$ is multiplied by a $\cos\phi$ or $\sin\phi$, while $\tilde{S}_{k,\beta}^{(1)}$ and $\tilde{S}_{k,\gamma}^{(1)}$ are multiplied by 1, $\cos 2\phi$, or $\sin 2\phi$. Therefore, we only need to keep terms dependent on $\cos\phi$, $\sin\phi$ in $\tilde{S}_{k,\alpha}^{(1)}$ and terms on 1, $\cos 2\phi$, $\sin 2\phi$ in $\tilde{S}_{k,\beta}^{(1)}$ and $\tilde{S}_{k,\gamma}^{(1)}$;

other terms will vanish upon integration over ϕ. Hence we show only the relevant terms that will give a nonvanishing contribution to the time-averaged longitudinal and Hall currents:

$$\tilde{S}_{k,\alpha}^{(1)} = \frac{1}{8k}\frac{eE}{D}\left\{4\mu\tau\Lambda\sin^2\theta_k\text{Im}\{S_k^T B_k^L\}\sin\phi + \left[4k\Lambda M_{k,+}\text{Re}\left\{\frac{\partial S_k^T}{\partial k}B_k^L\right\} + 8k\frac{\partial S_{k,0}}{\partial k}|B_k^L|^2\right]\cos\phi\right\}\cdots, \tag{B1}$$

$$\tilde{S}_{k,\beta}^{(1)} = \frac{1}{8k}\frac{eE}{D}\left\{\left[4\tau\Gamma M_{k,-}\text{Im}\{S_k^T B_k^L\} + 4\mu k\Gamma\text{Im}\left\{\frac{\partial S_k^T}{\partial k}B_k^L\right\} + 2k(2\alpha_k-\omega)M_{k,+}\Lambda\frac{\partial S_{k,0}}{\partial k} + kM_{k,+}^2\Lambda^2\frac{\partial S_{k,1}}{\partial k}\right]\right.$$

$$+ \left[-4\tau\Gamma M_{k,-}\text{Re}\{S_k^T B_k^L\} + 4\mu\Gamma k\text{Re}\left\{\frac{\partial S_k^T}{\partial k}B_k^L\right\} - 2\mu kM_{k,+}\Gamma_\perp\Lambda\frac{\partial S_{k,0}}{\partial k} - \mu\tau\sin^2\theta_k M_{k,+}\Lambda^2 S_{k,2}\right]\sin 2\phi$$

$$+ \left[-4\tau\Gamma M_{k,-}\text{Im}\{S_k^T B_k^L\} + 4\mu k\Gamma\text{Im}\left\{\frac{\partial S_k^T}{\partial k}B_k^L\right\} + 2k(2\alpha_k-\omega)M_{k,+}\Lambda\frac{\partial S_{k,0}}{\partial k} + kM_{k,+}^2\Lambda^2\frac{\partial S_{k,1}}{\partial k}\right]\cos 2\phi\right\}\cdots, \tag{B2}$$

$$\tilde{S}_{k,\gamma}^{(1)} = \frac{1}{8k}\frac{eE}{D}\left\{\left[4\mu\tau\Gamma M_{k,-}\text{Re}\{S_k^T B_k^L\} + 4k\Gamma\text{Im}\left\{\frac{\partial S_k^T}{\partial k}B_k^L\right\} - 2kM_{k,+}\Gamma_\perp\Lambda\frac{\partial S_{k,0}}{\partial k} + \tau\sin^2\theta_k M_{k,+}\Lambda^2 S_{k,2}\right]\right.$$

$$+ \left[-4\mu\tau\Gamma M_{k,-}\text{Re}\{S_k^T B_k^L\} + 4\Gamma k\text{Re}\left\{\frac{\partial S_k^T}{\partial k}B_k^L\right\} - 2kM_{k,+}\Gamma_\perp\Lambda\frac{\partial S_{k,0}}{\partial k} - \tau\sin^2\theta_k M_{k,+}\Lambda^2 S_{k,2}\right]\cos 2\phi$$

$$+ \left[4\mu\tau\Gamma M_{k,-}\text{Im}\{S_k^T B_k^L\} - 4k\Gamma\text{Im}\left\{\frac{\partial S_k^T}{\partial k}B_k^L\right\} - 2\mu k(2\alpha_k-\omega)M_{k,+}\Lambda\frac{\partial S_{k,0}}{\partial k} - \mu kM_{k,+}^2\Lambda^2\frac{\partial S_{k,1}}{\partial k}\right]\sin 2\phi\right\}\cdots, \tag{B3}$$

where $S_{k,0}, S_{k,1}, S_{k,2}$ are given in Eqs. (24), $M_{k,\pm}$ is defined under Eq. (37), and

$$S_k^T = S_{k,1} - iS_{k,2} = -\frac{\Lambda}{2}M_{k,+}\frac{(2\alpha_k-\omega)+i\mu\Gamma_\perp}{(2\alpha_k-\omega)^2 + \Gamma_\perp^2 + (\Lambda M_{k,+}/2)^2(\Gamma_\perp/\Gamma)}, \tag{B4}$$

$$B_k^L = (2\alpha_k - \omega) + i\mu\Gamma_\perp, \tag{B5}$$

and D is the determinant of the 3×3 matrix in Eq. (26),

$$D = \Gamma\left[\Gamma_\perp^2 + (2\alpha_k-\omega)^2 + \frac{\Gamma_\perp}{\Gamma}\left(\frac{\Lambda}{2}\right)^2 M_{k,+}^2\right]. \tag{B6}$$

APPENDIX C: $\tilde{S}_{k,\alpha}^{(1)}, \tilde{S}_{k,\beta}^{(1)}, \tilde{S}_{k,\gamma}^{(1)}$ CONTRIBUTIONS IN THE LONGITUDINAL AND HALL CONDUCTIVITIES

In Fig. 7, we display the contributions due to $\tilde{S}_{k,\alpha}^{(1)}, \tilde{S}_{k,\beta}^{(1)}, \tilde{S}_{k,\gamma}^{(1)}$ in the longitudinal [Eq. (36)] and Hall conductivities [Eq. (37)], which supplement our discussions on our results in Fig. 5.
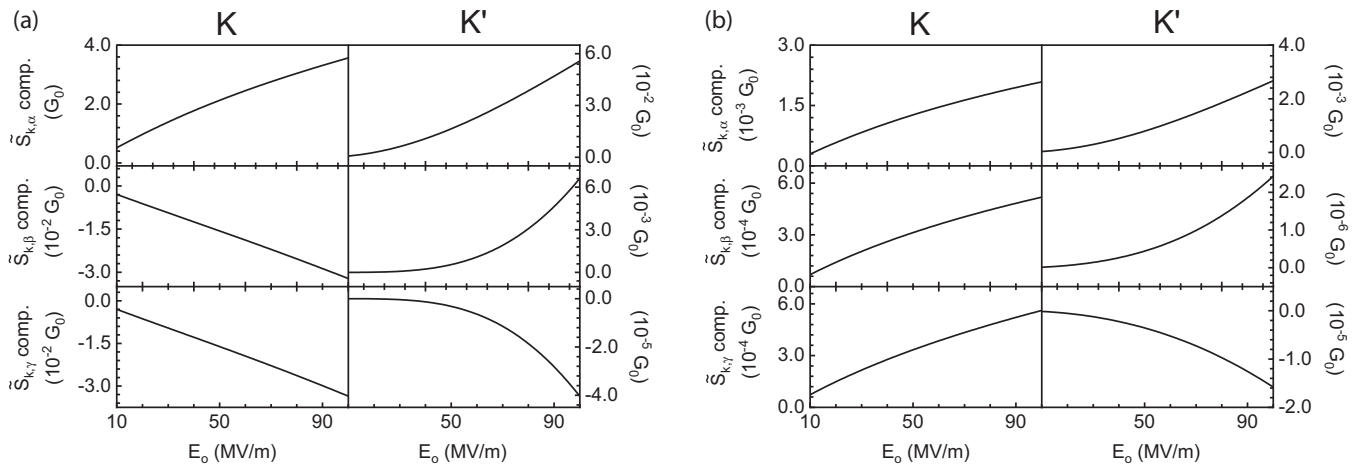

FIG. 7. Valley-specific conductivities (a) σ_{xx} and (b) σ_{yx} in units of $G_0 = e^2/\hbar$ as a function of the field strength E_0 for a pump field with frequency $\omega = 1.62$ eV and helicity $\mu = 1$. For each of σ_{xx} and σ_{yx}, the contribution from $\tilde{S}_{k,\alpha}^{(1)}$ is shown in the first row, $\tilde{S}_{k,\beta}^{(1)}$ in the second row, and $\tilde{S}_{k,\gamma}^{(1)}$ in the third row, whereas the two columns show the cases for valleys K and K'. Relaxation and dephasing rates are taken as $\Gamma = \Gamma_\perp = 1$ meV.

[1] K. S. Novoselov, A. K. Geim, S. V. Morozov, D. Jiang, Y. Zhang, S. V. Dubonos, I. V. Grigorieva, and A. A. Firsov, Electric field effect in atomically thin carbon films, Science **306**, 666 (2004).

[2] K. Novoselov, A. Mishchenko, A. Carvalho, and A. C. Neto, 2D materials and van der Waals heterostructures, Science **353**, aac9439 (2016).

[3] Z. Zhu, Y. Cheng, and U. Schwingenschlögl, Giant spin-orbit-induced spin splitting in two-dimensional transition-metal dichalcogenide semiconductors, Phys. Rev. B **84**, 153402 (2011).

[4] D. Xiao, G.-B. Liu, W. Feng, X. Xu, and W. Yao, Coupled Spin and Valley Physics in Monolayers of MoS$_2$ and other Group-VI Dichalcogenides, Phys. Rev. Lett. **108**, 196802 (2012).

[5] T. Cao, G. Wang, W. Han, H. Ye, C. Zhu, J. Shi, Q. Niu, P. Tan, E. Wang, B. Liu, and J. Feng, Valley-selective circular dichroism of monolayer molybdenum disulphide, Nat. Commun. **3**, 887 (2012).

[6] D. Xiao, W. Yao, and Q. Niu, Valley-Contrasting Physics in Graphene: Magnetic Moment and Topological Transport, Phys. Rev. Lett. **99**, 236809 (2007).

[7] W. Yao, D. Xiao, and Q. Niu, Valley-dependent optoelectronics from inversion symmetry breaking, Phys. Rev. B **77**, 235406 (2008).

[8] X. Dai and F.-C. Zhang, Light-induced Hall effect in semiconductors with spin-orbit coupling, Phys. Rev. B **76**, 085343 (2007).

[9] C. M. Yin, N. Tang, S. Zhang, J. X. Duan, F. J. Xu, J. Song, F. H. Mei, X. Q. Wang, B. Shen, Y. H. Chen, J. L. Yu, and H. Ma, Observation of the photoinduced anomalous Hall effect in GaN-based heterostructures, Appl. Phys. Lett. **98**, 122104 (2011).

[10] J. Yu, Y. Chen, C. Jiang, Y. Liu, H. Ma, and L. Zhu, Observation of the photoinduced anomalous Hall effect spectra in insulating InGaAs/AlGaAs quantum wells at room temperature, Appl. Phys. Lett. **100**, 142109 (2012).

[11] J. Yu, Y. Chen, Y. Liu, C. Jiang, H. Ma, L. Zhu, and X. Qin, Intrinsic photoinduced anomalous Hall effect in insulating GaAs/AlGaAs quantum wells at room temperature, Appl. Phys. Lett. **102**, 202408 (2013).

[12] J. Yu, Y. Chen, S. Cheng, X. Zeng, Y. Liu, Y. Lai, and Q. Zheng, Separation of the intrinsic and extrinsic mechanisms of the photo-induced anomalous Hall effect, Physica E **90**, 55 (2017).

[13] J. Yu, W. Wu, Y. Wang, K. Zhu, X. Zeng, Y. Chen, Y. Liu, C. Yin, S. Cheng, Y. Lai *et al.*, Giant photoinduced anomalous Hall effect of the topological surface states in three dimensional topological insulators Bi$_2$Te$_3$, Appl. Phys. Lett. **116**, 141603 (2020).

[14] P. Seifert, F. Sigger, J. Kiemle, K. Watanabe, T. Taniguchi, C. Kastl, U. Wurstbauer, and A. Holleitner, In-plane anisotropy of the photon-helicity induced linear Hall effect in few-layer WTe$_2$, Phys. Rev. B **99**, 161403(R) (2019).

[15] K. F. Mak, K. L. McGill, J. Park, and P. L. McEuen, The valley Hall effect in MoS$_2$ transistors, Science **344**, 1489 (2014).

[16] J. Lee, K. F. Mak, and J. Shan, Electrical control of the valley Hall effect in bilayer MoS$_2$ transistors, Nat. Nanotechnol. **11**, 421 (2016).

[17] J. W. McIver, B. Schulte, F.-U. Stein, T. Matsuyama, G. Jotzu, G. Meier, and A. Cavalleri, Light-induced anomalous Hall effect in graphene, Nat. Phys. **16**, 38 (2020).

[18] S. A. Sato, J. W. McIver, M. Nuske, P. Tang, G. Jotzu, B. Schulte, H. Hübener, U. De Giovannini, L. Mathey, M. A. Sentef, A. Cavalleri, and A. Rubio, Microscopic theory for the light-induced anomalous Hall effect in graphene, Phys. Rev. B **99**, 214302 (2019).

[19] T. Oka and H. Aoki, Photovoltaic Hall effect in graphene, Phys. Rev. B **79**, 081406(R) (2009).

[20] L. E. F. Torres, P. M. Perez-Piskunow, C. A. Balseiro, and G. Usaj, Multiterminal Conductance of a Floquet Topological Insulator, Phys. Rev. Lett. **113**, 266801 (2014).

[21] H. Dehghani, T. Oka, and A. Mitra, Out-of-equilibrium electrons and the Hall conductance of a Floquet topological insulator, Phys. Rev. B **91**, 155422 (2015).

[22] C.-K. Chan, P. A. Lee, K. S. Burch, J. H. Han, and Y. Ran, When Chiral Photons Meet Chiral Fermions: Photoinduced Anomalous Hall Effects in Weyl Semimetals, Phys. Rev. Lett. **116**, 026805 (2016).

[23] K. Taguchi, D.-H. Xu, A. Yamakage, and K. T. Law, Photo-voltaic anomalous Hall effect in line-node semimetals, Phys. Rev. B **94**, 155206 (2016).

[24] W.-R. Lee and W.-K. Tse, Dynamical quantum anomalous Hall effect in strong optical fields, Phys. Rev. B **95**, 201411(R) (2017).

[25] E. J. Sie, J. W. McIver, Y.-H. Lee, L. Fu, J. Kong, and N. Gedik, Valley-selective optical Stark effect in monolayer WS$_2$, Nat. Mater. **14**, 290 (2015).

[26] V. M. Galitskii, S. P. Goreslavskii, and V. F. Elesin, Electric and magnetic properties of a semiconductor in the field of a strong electromagnetic wave, Sov. Phys. JETP **30**, 117 (1970).

[27] S. Schmitt-Rink, D. S. Chemla, and H. Haug, Nonequilibrium theory of the optical Stark effect and spectral hole burning in semiconductors, Phys. Rev. B **37**, 941 (1988).

[28] Y. Wang, H. Steinberg, P. Jarillo-Herrero, and N. Gedik, Observation of Floquet-Bloch states on the surface of a topological insulator, Science **342**, 453 (2013).

[29] F. Mahmood, C.-K. Chan, Z. Alpichshev, D. Gardner, Y. Lee, P. A. Lee, and N. Gedik, Selective scattering between Floquet-Bloch and Volkov states in a topological insulator, Nat. Phys. **12**, 306 (2016).

[30] T. Oka and S. Kitamura, Floquet engineering of quantum materials, Annu. Rev. Condens. Matter Phys. **10**, 387 (2019).

[31] N. H. Lindner, G. Refael, and V. Galitski, Floquet topological insulator in semiconductor quantum wells, Nat. Phys. **7**, 490 (2011).

[32] R. Wang, B. Wang, R. Shen, L. Sheng, and D. Xing, Floquet Weyl semimetal induced by off-resonant light, Europhys. Lett. **105**, 17004 (2014).

[33] M. M. Asmar and W.-K. Tse, Floquet control of indirect exchange interaction in periodically driven two-dimensional electron systems, arXiv:2003.14383.

[34] M. Ke, M. M. Asmar, and W.-K. Tse, Non-equilibrium RKKY interaction in irradiated graphene, Phys. Rev. Research **2**, 033228 (2020).

[35] W.-R. Lee and W.-K. Tse, Photon-induced suppression of interlayer tunneling in van der Waals heterostructures, Phys. Rev. B **99**, 201403(R) (2019).

[36] K. Sacha and J. Zakrzewski, Time crystals: A review, Rep. Prog. Phys. **81**, 016401 (2017).

[37] V. Kovalev, W.-K. Tse, M. Fistul, and I. Savenko, Valley Hall transport of photon-dressed quasiparticles in two-dimensional Dirac semiconductors, New J. Phys. **20**, 083007 (2018).

[38] D. Culcer, E. H. Hwang, T. D. Stanescu, and S. Das Sarma, Two-dimensional surface charge transport in topological insulators, Phys. Rev. B **82**, 155457 (2010).

[39] D. Culcer and S. Das Sarma, Anomalous Hall response of topological insulators, Phys. Rev. B **83**, 245441 (2011).

[40] W.-K. Tse, Coherent magneto-optical effects in topological insulators: Excitation near the absorption edge, Phys. Rev. B **94**, 125430 (2016).

[41] H. Haug and S. W. Koch, *Quantum Theory of the Optical and Electronic Properties of Semiconductors: Fifth Edition* (World Scientific, Singapore, 2009).

[42] S. Sim, D. Lee, M. Noh, S. Cha, C. H. Soh, J. H. Sung, M.-H. Jo, and H. Choi, Selectively tunable optical Stark effect of anisotropic excitons in atomically thin ReS_2, Nat. Commun. **7**, 13569 (2016).

[43] E. J. Sie, C. H. Lui, Y.-H. Lee, L. Fu, J. Kong, and N. Gedik, Large, valley-exclusive Bloch-Siegert shift in monolayer WS_2, Science **355**, 1066 (2017).

[44] B. M. Fregoso, Y. H. Wang, N. Gedik, and V. Galitski, Driven electronic states at the surface of a topological insulator, Phys. Rev. B **88**, 155129 (2013).

[45] G. Usaj, P. M. Perez-Piskunow, L. E. F. Foa Torres, and C. A. Balseiro, Irradiated graphene as a tunable Floquet topological insulator, Phys. Rev. B **90**, 115423 (2014).

[46] T. Morimoto and N. Nagaosa, Topological nature of nonlinear optical effects in solids, Sci. Adv. **2**, e1501524 (2016).

[47] H. Haug and A.-P. Jauho, *Quantum Kinetics in Transport and Optics of Semiconductors* (Springer, Berlin, 2008), Vol. 2.

[48] J. Rammer and H. Smith, Quantum field-theoretical methods in transport theory of metals, Rev. Mod. Phys. **58**, 323 (1986).

[49] W.-K. Tse, A. Saxena, D. L. Smith, and N. A. Sinitsyn, Spin and Valley Noise in Two-Dimensional Dirac Materials, Phys. Rev. Lett. **113**, 046602 (2014).

[50] N. Nagaosa, J. Sinova, S. Onoda, A. H. MacDonald, and N. P. Ong, Anomalous Hall effect, Rev. Mod. Phys. **82**, 1539 (2010).

[51] N. Sinitsyn, Semiclassical theories of the anomalous Hall effect, J. Phys.: Condens. Matter **20**, 023201 (2007).

[52] M.-C. Chang and Q. Niu, Berry curvature, orbital moment, and effective quantum theory of electrons in electromagnetic fields, J. Phys.: Condens. Matter **20**, 193202 (2008).

[53] C. H. Wong and Y. Tserkovnyak, Quantum kinetic equation in phase-space textured multiband systems, Phys. Rev. B **84**, 115209 (2011).

[54] D. Culcer, A. Sekine, and A. H. MacDonald, Interband coherence response to electric fields in crystals: Berry-phase contributions and disorder effects, Phys. Rev. B **96**, 035106 (2017).

[55] M. Massicotte, F. Vialla, P. Schmidt, M. B. Lundeberg, S. Latini, S. Haastrup, M. Danovich, D. Davydovskaya, K. Watanabe, T. Taniguchi *et al.*, Dissociation of two-dimensional excitons in monolayer WSe_2, Nat. Commun. **9**, 1 (2018).

[56] N. Ubrig, S. Jo, M. Philippi, D. Costanzo, H. Berger, A. B. Kuzmenko, and A. F. Morpurgo, Microscopic origin of the valley Hall effect in transition metal dichalcogenides revealed by wavelength-dependent mapping, Nano Lett. **17**, 5719 (2017).

[57] W.-K. Tse and A. H. MacDonald, Interaction effects in the optical conductivity of bilayer graphene: Drude-interband coupling and screening, Phys. Rev. B **80**, 195418 (2009).

[58] S. H. Abedinpour, G. Vignale, A. Principi, M. Polini, W.-K. Tse, and A. H. MacDonald, Drude weight, plasmon dispersion, and ac conductivity in doped graphene sheets, Phys. Rev. B **84**, 045429 (2011).

[59] X. Li and W.-K. Tse, Theory of interaction-induced renormalization of Drude weight and plasmon frequency in chiral multilayer graphene, Phys. Rev. B **95**, 085428 (2017).

[60] T. Wehling, A. M. Black-Schaffer, and A. V. Balatsky, Dirac materials, Adv. Phys. **63**, 1 (2014).

[61] N. P. Armitage, E. J. Mele, and A. Vishwanath, Weyl and Dirac semimetals in three-dimensional solids, Rev. Mod. Phys. **90**, 015001 (2018).

[62] M. Z. Hasan and C. L. Kane, Colloquium: Topological insulators, Rev. Mod. Phys. **82**, 3045 (2010).